Superconductor Science and Technology

Development and performance of a 2.9 Tesla dipole magnet using high-temperature superconducting CORC® wires

To cite this article before publication: Xiaorong Wang *et al* 2020 *Supercond. Sci. Technol.* in press https://doi.org/10.1088/1361-6668/abc2a5

Development and performance of a 2.9 Tesla dipole magnet using high-temperature superconducting CORC® wires

Xiaorong Wang[1], Dmytro Abraimov[2], Diego Arbelaez[1], Timothy J. Bogdanof[1], Lucas Brouwer[1], Shlomo Caspi[1], Daniel R. Dietderich[1], Joseph DiMarco[3], Ashleigh Francis[2], Laura Garcia Fajardo[1], William B. Ghiorso[1], Stephen A. Gourlay[1], Hugh C. Higley[1], Maxim Marchevsky[1], Maxwell A. Maruszewski[1], Cory S. Myers[1,4], Soren O. Prestemon[1], Tengming Shen[1], Jordan Taylor[1], Reed Teyber[1], Marcos Turqueti[1], Danko van der Laan[5,6], Jeremy D. Weiss[5,6]

[1] Lawrence Berkeley National Laboratory, Berkeley, CA 94720, USA
[2] Applied Superconductivity Center, National High Magnetic Field Laboratory, Florida State University, Tallahassee, FL 32310, USA
[3] Fermi National Accelerator Laboratory, Batavia, IL 60510, USA
[4] Ohio State University, Columbus, OH 43210, USA
[5] Advanced Conductor Technologies, Boulder, CO 80301, USA
[6] University of Colorado, Boulder, CO 80309, USA

E-mail: xrwang@lbl.gov

Abstract. Although the high-temperature superconducting (HTS) $REBa_2Cu_3O_x$ (REBCO, RE = rare earth elements) material has a strong potential to enable dipole magnetic fields above 20 T in future circular particle colliders, the magnet and conductor technology needs to be developed. As part of an ongoing development to address this need, here we report on our CORC® canted $\cos\theta$ magnet called C2 with a target dipole field of 3 T in a 65 mm aperture. The magnet was wound with 70 m of 3.8 mm diameter CORC® wire on machined metal mandrels. The wire had 30 commercial REBCO tapes from SuperPower Inc., each 2 mm wide with a 30 μm thick substrate. The magnet generated a peak dipole field of 2.91 T at 6.290 kA, 4.2 K. The magnet could be consistently driven into the flux-flow regime with reproducible voltage rise at an engineering current density between 400 – 550 A mm^{-2}, allowing reliable quench detection and magnet protection. The C2 magnet represents another successful step towards the development of high-field accelerator magnet and CORC® conductor technologies. The test results highlighted two development needs: continue improving the performance and flexibility of CORC® wires and develop the capability to identify locations of first onset of flux-flow voltage.

1. Introduction

High-temperature superconductors such as $Bi_2Sr_2CaCu_2O_{8+x}$ (Bi-2212) and $REBa_2Cu_3O_{7-\delta}$ (REBCO, RE = rare earth elements) can enable future magnets capable of generating dipole fields above 20 T. The Bi-2212 front has demonstrated several aspects of the high-field accelerator magnet technology such as the engineering current density (J_e), filament size, Rutherford cable technology, magnet fabrication, operation and protection [1–8]. One engineering issue that is being addressed is the heat treatment of coils under high pressure [3, 8]. Although REBCO conductors feature attractive current-carrying capability over a wide range of temperature and magnetic field [9, 10], the REBCO front also has significant development needs to address [7].

For instance, an optimum REBCO conductor design capable of carrying currents in excess of 5 kA remains to be determined and how we can use it to generate dipole fields above 20 T remains to be addressed. Two primary multi-tape architectures have emerged as candidate magnet conductors in the past few years. One is the stacked-tape architecture such as the Roebel [11], twisted-stack [12], and exfoliated REBCO cables [13]. The other is the round-wire architecture with tapes helically wrapped around a core, such as CORC® [14, 15] and STAR™ wires [16]. Comprehensive comparisons of various cable designs for accelerator magnet applications can be found in [17, 18].

The EuCARD and EuCARD2 collaborations in Europe successfully demonstrated first integration of REBCO cables into model racetrack and dipole coils. A 5.37 T dipole field at 4.2 K was achieved in a racetrack coil wound with a stack of two isolated REBCO tapes, each tape possessing two REBCO layers and additional CuBe2 tape stabilizers [19, 20]. Based on Roebel cables, a series of aligned block dipole magnets with a 40 mm aperture demonstrated a 3.35 T dipole field at 5 K (FeatherM2.12) and 4.2 T at 4.5 K (FeatherM2.34) [21–23].

The U.S. Magnet Development Program (MDP) [24], supported by the Office of High Energy Physics at the U.S. Department of Energy, is collaborating with Advanced Conductor Technologies LLC (ACT) on CORC® canted $\cos\theta$ (CCT) magnets [25–30] as a vehicle to develop REBCO accelerator magnet technology for the round-wire architecture. Magnet fabrication and performance also provides feedback for the CORC® conductor development. Our ultimate goal is to generate a dipole field of 20 T when combining a CORC®-based CCT insert magnet with a low-temperature superconducting (LTS) magnet. Several model magnets will be developed, generating increasing self-dipole fields, before a CORC® insert magnet generating 5 T in a background field of 15 T from an LTS magnet will be developed. Each model magnet is based on a higher performing CORC® wire wound from REBCO tapes with higher in-field performance, and would address key issues in magnet technology.

A two-layer CCT dipole magnet named C1 was developed as the first step with a target dipole field of 1 T at 4.2 K [31]. It used a CORC® wire with a low J_e of about 150 A mm^{-2} at 4.2 K, 20 T. The C1 magnet successfully demonstrated the concept of a CCT dipole magnet using CORC® wires, allowing for the next step in the CCT

dipole magnet development wound from CORC® wires with higher in-field performance to help address questions including:

(i) How can we develop the CCT technology to generate higher dipole fields where significant Lorenz forces require stronger mandrels than the 3D printed non-metal mandrel as was done in C1?

(ii) How to develop CORC® wires with the required performance to achieve higher dipole fields, ensuring that their in-field performance is consistent over long lengths exceeding 20 meters?

(iii) What can we learn from such a magnet regarding their quench behavior and field quality?

(iv) And finally, what key conductor and magnet developments need to become available to enable the next magnets to generate even higher dipole fields?

To help address these questions, we made the C2 magnet with a four-layer CCT design and a target dipole field of 3 T at 4.2 K. Here we report on the development and performance of the C2 magnet and its three-turn subscale version. The C2 magnet was wound from 70 m of CORC® wire. The 30-tape wire contained 2 mm wide REBCO tapes with a 30 μm thick substrate, resulting in an expected wire J_e of about 250 A mm^{-2} at 4.2 K, 20 T. The magnet used machined aluminum bronze mandrels to support the wires. Stycast 2850 MT with fiberglass tape was applied after winding to constrain the conductors. The C2 magnet reached a maximum dipole field of 2.91 T at 4.2 K. The development and testing of this magnet also allowed us to study the quench behavior and field quality of CORC® CCT magnets with higher dipole fields and higher conductor J_e. The C2 magnet provided important feedback on the REBCO conductor and magnet technology towards reaching higher dipole fields within the MDP roadmap. The development of the C2 magnet also highlighted the need to continue improving the transport performance and flexibility of the CORC® wire and other magnet development needs.

2. Conductor, magnet design and fabrication

2.1. CORC® wire

ACT fabricated the CORC® wires in August 2018 using commercial SuperPower REBCO tapes with a 30 μm thick substrate [32]. The original wire design had 27 tapes, which was based on the expected in-field performance of the 2 mm wide REBCO tapes to be close to the average critical current (I_c) of between 300 and 350 A at 4.2 K, 5 T, of similar tapes measured earlier. The measurements performed at the Applied Superconductivity Center/National High Magnetic Field Laboratory showed that the in-field transport current of several tapes was lower than expected, with a larger portion of the tapes having an I_c of between 250 and 300 A at 4.2 K, 5 T. To ensure the magnet performance, we increased the number of tapes from 27 to 30 for the final

wire layout. CORC® wires with a total length of 100 m were fabricated using 5 km of REBCO tape. A 10 m long wire was used for the three-turn subscale coils. The 40-turn C2 magnet consumed the remaining 90 m long wires, including 20 m for short-sample measurements, winding practice and leader wire for winding. Table 1 gives the main parameters of the wire used for the C2 magnet.

Table 1. Main parameters of the CORC® wires used for the 40-turn C2 magnet.

		CCT layer			
Parameter	Unit	1	2	3	4
Tape vendor	-	SuperPower Inc.			
Number of tapes	-	30			
Layers of tapes inside wire	-	12			
Tapes per wire layer	-	2 or 3			
Tape width	mm	2			
Substrate thickness	μm	30			
Cu plating thickness per tape side	μm	5			
Average tape I_c, 77 K, self-field	A	76	73	72	60
Standard deviation of tape I_c with respect to the average, 77 K, self-field	-	6%	7%	12%	16%
Fabricated wire length	m	18	20	24	28
Insulated wire diameter	mm	3.80	3.80	3.77	3.67
Polyester insulation thickness	μm	30			
Diameter of Cu core	mm	2.54			
Cu to non-Cu ratio	-	1.0			
Cu termination length	mm	200			
Cu termination outer diameter	mm	7.94			

The I_c of a 2 m long sample from the Layer 1 wire was measured in different background fields at 4.2 K as a witness sample to help determine the expected magnet performance (see § 4.2.2). The sample was wound for three turns around a 63 mm diameter sample holder.

2.2. Magnet design and fabrication

The C2 magnet contains four layers (coils) and has a clear aperture of 65 mm. Figure 1 shows a side view of the four layers and their lead arrangement. Table 2 gives the main design parameters of the magnet.

The layer design for the 40-turn C2 magnet was modified based on the winding experience from the three-turn subscale magnet. The reverse bends of the exit leads in the subscale magnet design was an issue (figure 2(a)), where the 30-tape CORC® wire in these regions would not stay in the groove without external constraint. Stycast was

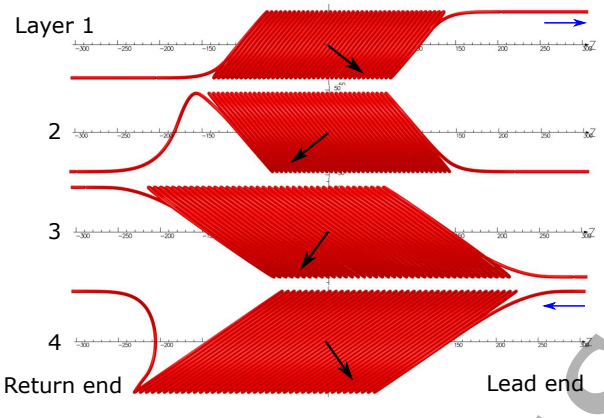

Figure 1. Arrangement of the four layers for the C2 magnet (to scale). The horizontal scale ranges from −300 to 300 mm. The current flows into the magnet from the lead end of Layer 4 and comes out at the lead end of Layer 1. The arrows at the coil center indicate the field direction.

Table 2. Main design parameters for the C2 magnet.

		CCT layer			
Design parameters	Unit	1	2	3	4
Inner diameter (ID)	mm	65.00	84.25	98.45	112.65
Wire center diameter	mm	78.10	92.30	106.50	120.70
Outer diameter (OD) at mandrel ends	mm	84.07	98.27	112.47	127.00
Spar thickness	mm	4.50	1.98	1.98	1.98
Wire turns	-	40			
Wire length	m	12.5	14.6	19.7	22.5
Groove diameter	mm	4.1			
Gap between wires at the mid-plane	mm	0.23	0.23	0.32	0.37
Wire tilt angle at the mid-plane	degree	50	−50	−35	35
Minimum bending radius of the wire center line	mm	30	35	30	35
Contribution to the dipole field	-	22%	22%	28%	28%
Mandrel length	mm	613			
Mandrel material	-	aluminum bronze 954			
Short-sample prediction (SSP) at 4.2 K	kA	6.392			
Aperture dipole field at the SSP	T	3.02			
Aperture dipole field transfer function	T kA^{-1}	0.473			
Peak conductor field at the SSP	T	3.38	3.39	2.98	2.53
Magnet inductance per unit magnetic length	mH m^{-1}	2.0			
Magnet stored energy at the SSP	kJ m^{-1}	41			

applied to constrain the wire in the reverse bends in the subscale coil before resuming, which caused additional wire handling and slowed the coil fabrication. The design of the C2 magnet removed the reverse bends by changing the orientation of Layers 3 and

4 and modifying the exit lead design (figure 2(b)).

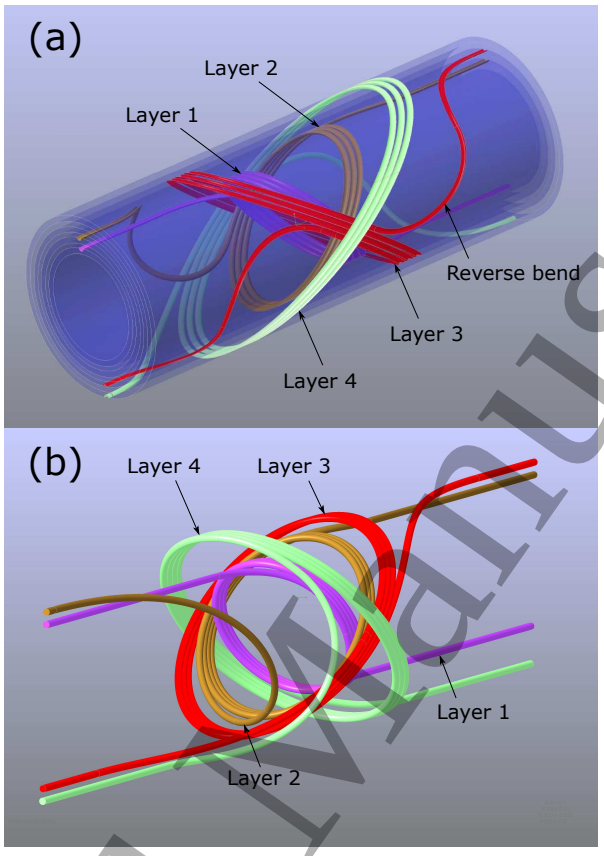

Figure 2. (a) The first design that was used in the three-turn subscale magnet. The design also has reverse bends in Layers 2, 3 and 4. (b) The modified design that was used in the C2 magnet with no reverse bends.

We considered three different groove designs for the C2 magnet (figure 3). Although Design A was most convenient for winding a CORC® CCT coil as demonstrated for the C1 magnet [31], a five-axis CNC machine would be required to make such a groove on a metal mandrel with a limited mandrel length (< 300 mm). The radial groove (Designs B and C) can be machined with an in-house four-axis CNC machine for a mandrel up to 1 m long. The winding test with Design B using the existing winding table proved to be challenging, especially when the CORC® wire was under tension. Therefore, the final design used Design C, a half-depth radial groove, as a compromise between the groove machining and coil winding. Although a full-depth groove may be required to support the conductor in a high-field design, it was not an issue for the C2 magnet. Ensuring a uniform outer profile of the coil with wet Stycast was a concern for the half-depth groove. Figure 4 shows the coil winding and a close-up view of the wire in the half-depth groove.

The three-turn subscale magnet used Accura® Bluestone™ printed mandrels and the C2 magnet used mandrels made of aluminum bronze 954 alloy. The mandrels had raised ends to support concentric layers without compromising the CORC® wires. A

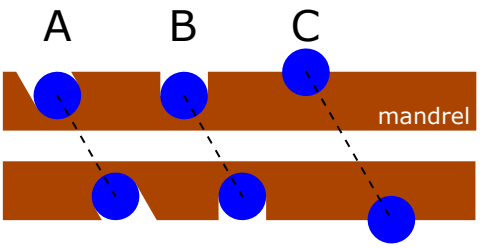

Figure 3. A longitudinal cross section of a mandrel showing wires in three different groove designs at the pole region. A: full-depth tilted groove; B: full-depth radial groove; C: half-depth radial groove.

Figure 4. (a) Winding Layer 2 using the existing winding table [31]. (b) CORC® wire enters the half-depth groove.

small radial clearance between the layers was used, which avoided needing spacers to radially center the layers. Longitudinal grooves were machined in the raised ends of each mandrel to allow cryogens to penetrate the gap between mandrels.

Before winding coils, a Cu termination was installed on one end of the CORC® wire with molten indium, following the procedure reported earlier [31, 33]. The termination was made of an oxygen-free C10100 Cu tube (table 1). During winding, the mandrel was attached to a tilted beam such that the grooves and the incoming wires were aligned on a horizontal plane while the mandrel traveled along the beam (figure 4 (a)). A winding tension of 30 N was applied to the CORC® wire. The second termination was installed after the winding was completed.

When winding Layer 1, we detected several electrical shorts between the CORC® wire and the mandrel by continuously monitoring the electrical resistance between them. A short appeared when the edge of the metal groove cut through the wire insulation and touched the REBCO tapes (figure 4(b)). Some shorts disappeared once the wire settled into the groove. The remaining shorts were removed by inserting a piece of Kapton tape between the wire and groove. The edges of the groove in the other three layers were further manually rounded and polished before winding. Table 3 gives the room-temperature electrical resistance between the wire and mandrel after winding.

A triplet of solid Cu instrumentation wires (MWS Twistite® 0.202 mm diameter) was used to monitor layer voltage. Each wire brought a voltage tap from the return

Table 3. Room-temperature electrical resistance between the wire and mandrel after winding.

CCT Layer	1	2	3	4
Resistance (Ω)	> 60 M	435	> 60 M	3.3 M

end termination to the lead end (see section 3.1). For the subscale three-turn magnet, the triplet was completely co-wound with the CORC® wires in Layer 1 but was only partially co-wound in the other three layers. For the 40-turn C2 magnet, the triplet was completely co-wound with the CORC® wire. An ultraviolet-activated glue was used to fix the triplet to the CORC® wire when needed.

The final step of the coil fabrication was to apply and cure Stycast epoxy (2850 MT) to constrain and support the CORC® wires. When painting Stycast on the coil surface, we wrapped a layer of fiberglass tape (W1132205, Carolina Narrow Fiber) tightly around the coil to enhance the strength of the cured Stycast. To ensure a uniform final coil surface for magnet assembly, a heat-shrink tape was wrapped and shrunk around the fiberglass and wet Stycast layer. The release-coated heat-shrink tape was removed after the Stycast was cured. Figure 5 shows all four layers of the C2 magnet before assembly.

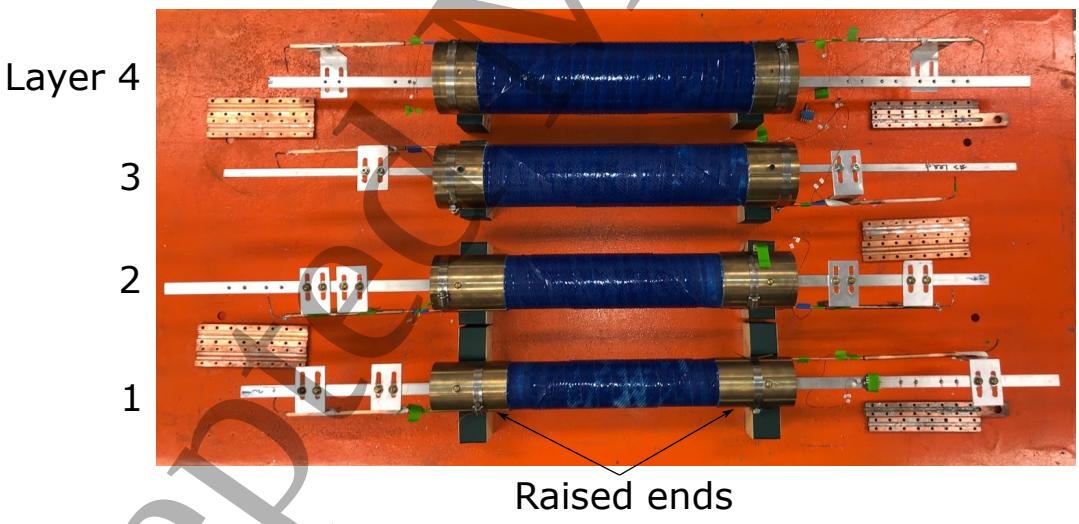

Figure 5. Four layers of the C2 magnet before assembly. The Cu termination blocks for the joints are grouped next to the CORC® wire terminations.

2.3. Magnet assembly

The magnet was assembled by inserting the inner layers into the outer layers. Due to the relatively low electrical resistance between the conductor and mandrel in Layers 2 and 4 (table 3), we covered the raised ends of the inner layers with Kapton tape to electrically isolate the metal mandrels. The first attempt with a 50 μm thick Kapton tape failed. It was too thick for the actual radial clearance between the layers. The

second attempt with a nominally 38 μm thick adhesive Kapton tape succeeded.

Figure 6 shows the assembled layers viewed from the return end of the magnet. To align the layers in the longitudinal and azimuthal directions, stainless steel pins were inserted into the alignment holes on the mandrels. Each pin has a Garolite CE jacket to prevent electrical connection between the mandrels.

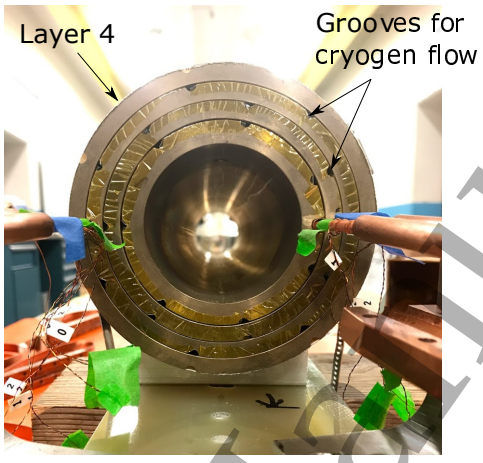

Figure 6. The view from the return end of the C2 magnet with a 65 mm clear aperture. The Kapton tapes on the inner three layers are visible.

After confirming that there was no electrical short between the layers following the assembly, we mounted the assembled layers to a G10 board to make the current leads and inter-layer electrical joints based on the practice and feedback from the subscale magnet. The leads and joints consisted of a pair of mating Cu blocks with grooves (figure 5), indium foils and CORC® terminations. We first covered the mating surfaces of both Cu blocks and the inner surface of the grooves with 130 μm thick indium foils (Lakeshore IF-5). Then we sandwiched the CORC® termination between the Cu blocks. Through a bolted connection of the Cu blocks, a pressed contact was formed between the Cu block and CORC® termination.

The current leads and joints were mechanically anchored to the G10 board to strain relieve the conductor. Flexible Nb-Ti Rutherford cables were used to connect the current leads to the test header. Figure 7 shows the C2 magnet after assembly. The magnet was positioned vertically after being attached to the test header.

3. Experimental setup and measurement protocol

3.1. Instrumentation

Voltage taps (VT) were installed inside the CORC® terminations to measure the voltage across each layer (figure 8). Three voltage signals were recorded for each layer: V_0 between VT A and F that were soldered on the Cu core outside the termination, V_1 between VT B and E that were installed close to the center of the Cu termination, and V_2 between VT C and D that were installed about 5 mm within the Cu termination.

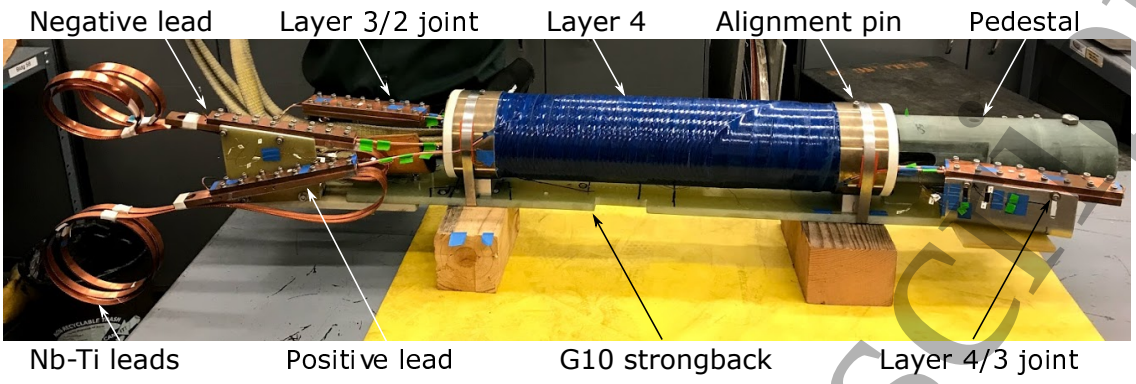

Figure 7. The C2 magnet before being attached to the test stand. The contour of the CORC® wires is visible.

The voltage across the inter-layer praying-hand joint was measured between VT D for the Layer 1/2 joint and Layer 3/4 joint; and between VT C for the Layer 2/3 joint.

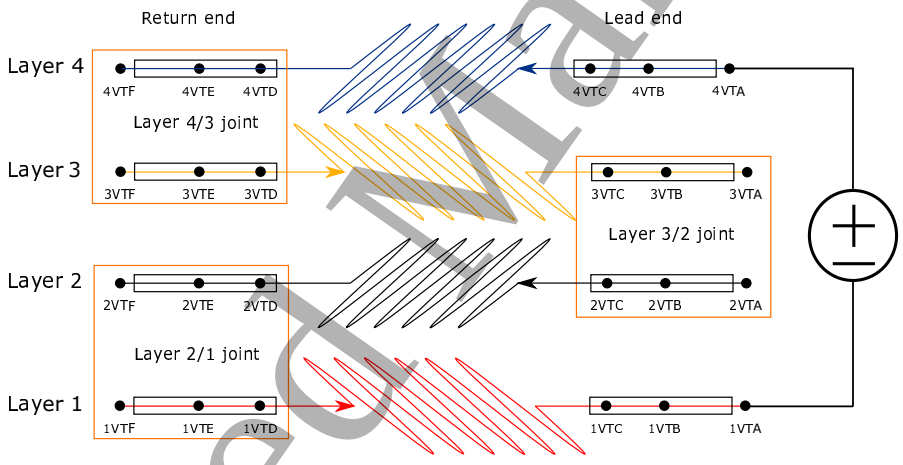

Figure 8. The voltage tap configuration for the three-turn subscale magnet and the C2 magnet. The black boxes are terminations. The orange boxes indicate the inter-layer joints. The arrows indicate the direction of transport current.

All three voltage signals from each layer were digitized by National Instruments 9238 input modules at a sampling rate of 1.6 kHz. The voltage signals from the three-turn subscale magnet were digitized with a National Instruments SCXI system at a rate of 1 kHz. The V_2 voltage signals were also measured with Keithley 2182A nanovoltmeters at a rate of 1 Hz. Voltages across the Nb-Ti current leads and vapor-cooled leads were measured with a Keithley 2001 digital multimeter.

The magnet was connected to a 25 kA DC power supply with the current measured with a precision shunt. The analog output from the nanovoltmeters with a gain of 1000 were connected to a quench detection system. The power supply current ramped down to zero when the layer voltage exceeded threshold values for the quench detection. No external energy-extraction resistor was used.

A cryogenic Hall sensor (Lakeshore HGCT3020) was mounted at the aperture center

of the three-turn subscale magnet to measure its dipole field. We used the standard measurement technique based on a rotating coil [34] to measure the field quality of the 40-turn C2 magnet. The rotating coil was developed by Fermi National Accelerator Laboratory based on printed-circuit board (PCB) technology [35]. The PCB circuit is 100 mm long and the outermost circuit trace has a radius of 21.55 mm. An anticryostat with an outer diameter of 63.5 mm was inserted into the magnet to house the rotating coil. The positioning accuracy of the rotating coil is 0.1 mm. The resolution of the rotating coil is 10^{-5} of the main dipole field at the radius of 21.55mm. More details about the measurement setup can be found in [36, 37].

The cryogen level was monitored and maintained during the test to cover the magnet and joints. To monitor the temperature inside the cryostat during the cooldown, we mounted a calibrated Cernox® temperature sensor next to the lead-end joints and attached a Platinum temperature sensor to the bottom plate that supported the magnet. The temperature readings also helped to indicate the level of cryogen during the tests.

3.2. Measurement goals and protocol

The three-turn subscale magnet provided necessary experience for the development of the 40-turn C2 magnet. Measuring the coil performance at 77 and 4.2 K allowed us to verify the coil fabrication and magnet assembly procedure, joint fabrication, and integration with the test stand. We also wanted to quantify the impact of coil fabrication and handling on the magnet transport performance by measuring the wire I_c before winding and after each step of the coil fabrication, in particular after winding and applying Stycast epoxy (figure 9).

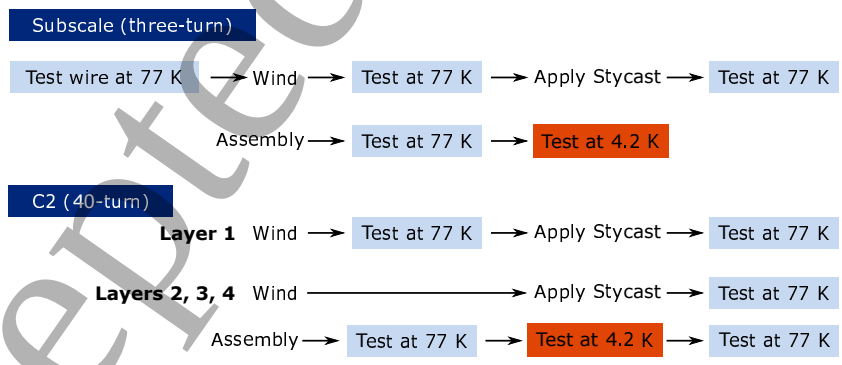

Figure 9. Measurement protocol for the three-turn subscale magnet and the C2 magnet.

Before winding, we cut the wire to the length for each coil and installed the terminations with voltage taps. The wire was then mounted on a sample holder to measure the I_c before winding (figure 10). The conductor was wound into a circle with a diameter of 250 – 300 mm to avoid bending degradation on the wire. The gap between the neighboring turns was at least 25 mm to minimize the impact of magnetic fields from

the neighboring turns. After the I_c measurement, the same wires with terminations were wound into three-turn subscale coils.

Figure 10. A CORC® wire for a three-turn subscale coil mounted on a sample holder for the I_c measurement before winding.

The subscale magnet was tested twice at 77 K with a warmup to room temperature between the tests. Following the second 77 K test, the subscale magnet was tested at 4.2 K without being warmed up to room temperature.

The goal of the C2 magnet test was to reach a 3 T dipole field through improvements in conductor performance and further development of the CCT magnet technology beyond that of the previous C1 magnet. The $V(I)$ transition was first measured for each layer at 77 K after fabrication to assess the coil performance. For Layer 1, one additional transport measurement was performed before applying Stycast epoxy to determine how the application of Stycast affected the performance of a 40-turn coil on a metal mandrel (figure 9). The transport performance and field quality of the C2 magnet were measured at 77 and 4.2 K. After warming up from 4.2 K to room temperature, the magnet was tested again at 77 K.

Two kinds of measurements using a rotating coil were performed to study the field quality of the C2 magnet. The first kind included measuring the field at different positions along the magnet. One full set of measurements along the magnet, at a given temperature, is considered a scan. We performed scans at constant currents at 280, 77, and 4.2 K to study the persistent-current and geometric effects. The scan at 280 K, performed after the second 77 K test, used a current of 5 A to limit the current density to 1 A mm^{-2} in the Cu core of the CORC® wire. The second kind of measurement

involved measuring the ramp-rate dependence of the field quality at 77 and 4.2 K at the magnetic center during current ramping. The probe rotated at a speed of 3 Hz for all the measurements.

4. Results

4.1. The three-turn subscale magnet

Six three-turn coils were fabricated and tested: four with 3D printed Bluestone™ mandrels and two with machined aluminum bronze mandrels. The subscale magnet contained four coils on the Bluestone™ mandrels.

4.1.1. I_c retention at different fabrication steps Figure 11 shows an example of $V_2(I)$ for the wire wound on a Bluestone™ mandrel.

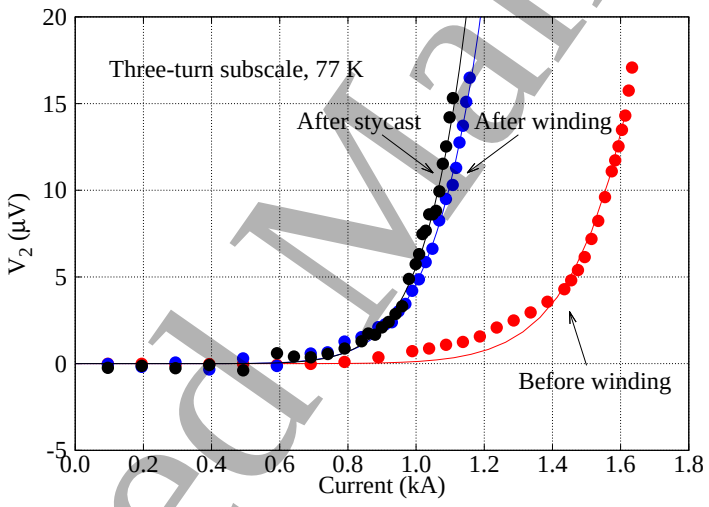

Figure 11. V_2 (see section 3.1) as a function of current for a wire used in a three-turn coil on a Bluestone™ mandrel before and after winding, and after applying Stycast. The measurements were performed at 77 K in self-field. The lines are a power-law fit according to (1).

A power-law fit was used to characterize the measured $V(I)$ data, as given by

$$V = V_o + IR + V_c \left(\frac{I}{I_c}\right)^n, \quad (1)$$

where V_o is the voltage offset, R is the termination resistance, and V_c is the voltage criterion. With a voltage criterion of 20 μV, corresponding to a maximum electric field of 14 μV m^{-1} for each layer of the three-turn subscale magnet, the data shown in figure 11 give an I_c and n-value of 1,671 A and 12.0 before winding, 1,189 A and 9.6 after winding, and 1,148 A and 9.3 after applying Stycast epoxy.

Figure 12 shows the $V(I)$ transition of each individual layer before and after the subscale magnet was assembled. The transport measurements of six subscale layers

revealed an average I_c reduction of 27% after winding, with a standard deviation of 5% at 77 K, self-field (table 4). Applying the Stycast epoxy and heat-shrink tape caused up to 3% I_c reduction. The I_c decreased by 48% on average at 77 K after assembly with four layers operating as a whole magnet.

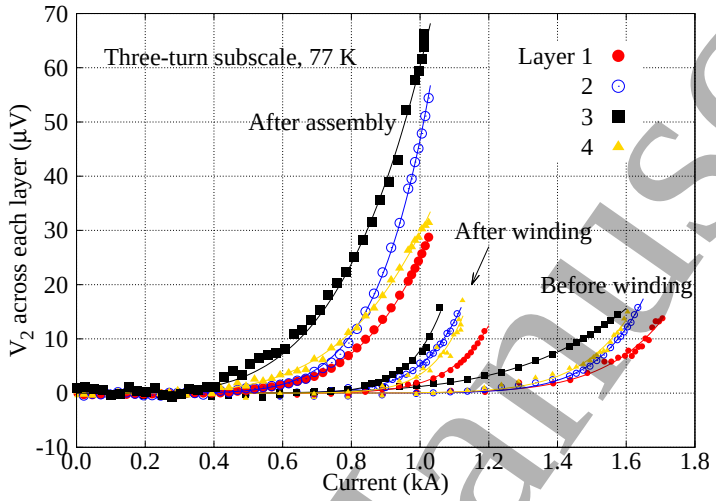

Figure 12. $V_2(I)$ across each layer of the three-turn subscale magnet before and after winding, and after assembly into the four-layer subscale magnet. The measurements were performed at 77 K. Lines are the fitting of the experimental data according to (1).

Table 4. I_c and n-value of each three-turn subscale coil at 77 K. I_c and n-value are determined at 20 μV criterion according to (1). "BS" denotes Bluestone™ and "AB" denotes aluminum bronze.

	77 K		77 K		77 K		77 K		4.2 K		4.2/77 K
Layer	Before winding		After winding		After Stycast		After assembly		After assembly		ratio
	I_c (A)	n (-)	I_c (A)	n (-)	I_c (A)	n (-)	I_c (A)	n (-)	I_c (A)	n (-)	(-)
BS 1	1,777	10.0	-	-	1,255	11.1	958	5.5	10,897	4.6	11.4
BS 2	1,671	12.0	1,189	9.6	1,148	9.3	878	6.5	7,996	4.9	9.1
BS 3	1,671	5.6	1,132	10.6	1,091	11.2	774	4.2	7,997	5.4	10.3
BS 4	1,669	10.0	1,157	12.0	-	-	911	4.2	8,274	4.0	9.1
AB 1	1,514	4.6	1,223	10.3	1,201	10.1	-	-	-	-	-
AB 3	1,522	9.9	1,137	15.9	1,132	14.6	-	-	-	-	-

4.1.2. Transport performance at 4.2 K Figure 13 shows the $V(I)$ curves across each layer of the subscale magnet at 4.2 K measured during a current ramp with a constant rate of 15 A s^{-1}. The subscale magnet generated a dipole field of 0.94 T at 8.5 kA with an engineering current density of 750 A mm^{-2}. The voltage signals had different peak-to-peak amplitudes of inductive noise: 34 μV for Layer 1, 500 μV for Layer 2,

700 μV for Layer 3, and 810 μV for Layer 4, all based on the raw voltage data. The electrical resistances across the inter-layer joints were also measured (see § 4.3).

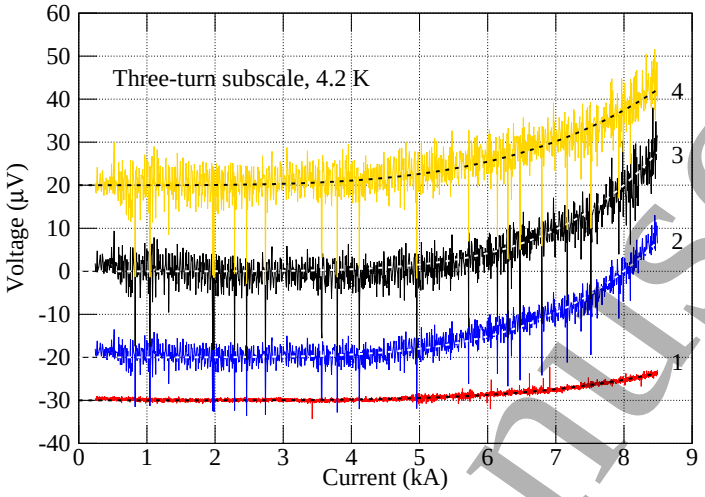

Figure 13. $V_2(I)$ measured across each layer of the three-turn subscale magnet at 4.2 K, self-field. The data were averaged from the raw voltage data. The curves are offset along the y-axis to highlight the inductive noise level. The dashed lines are the exponential fit according to (1).

Table 4 shows the I_c and n-value of each layer in the three-turn subscale magnet at 4.2 K, defined at 20 μV voltage criterion. The last column in table 4 gives the I_c ratio between the 4.2 and 77 K after assembly.

4.2. The 40-turn C2 magnet

4.2.1. Transport performance at 77 K The I_c and n-value of Layer 1 of the C2 magnet remained the same before and after applying Stycast epoxy. Therefore, we skipped the test at 77 K after applying Stycast for the other three layers. The C2 magnet was cooled down from room temperature to 77 K at a rate of less than 2 K per minute.

Figure 14 shows the voltage of each layer stand-alone and after assembly at 77 K. Layer 4 had the lowest performance followed by Layer 1. Table 5 summarizes the I_c and n-value of each layer determined at the 20 μV voltage criterion, which corresponds to an electric field criterion of 1.6 μV m^{-1} for Layer 1 and 0.9 μV m^{-1} for Layer 4.

4.2.2. Transport performance at 4.2 K A 100 mA current was applied to the magnet during the cooldown to monitor the superconducting transition of each layer. Figure 15 shows the transition of each layer during the cooldown to 4.2 K with helium gas. The transition occurred sequentially from the outer to inner layers (figure 6).

Figure 16 shows the voltage across each layer during the ramp reaching the maximum current of 6.290 kA and a dipole field of 2.91 T. Layer 4 again showed the lowest transport performance. The I_c and n-value of each layer are reported in table 5.

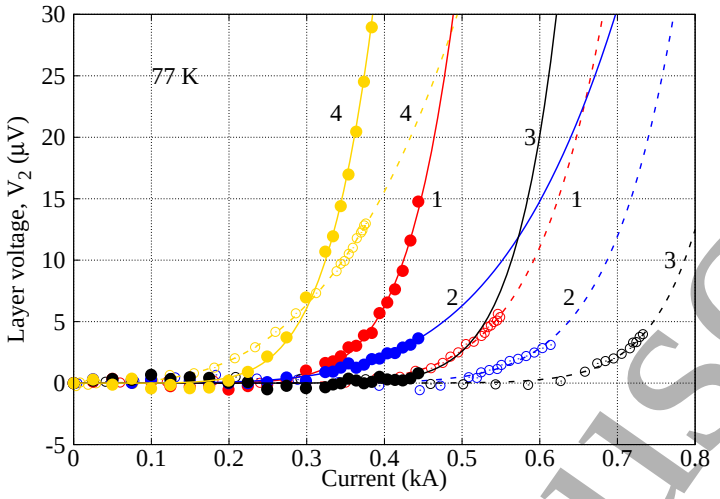

Figure 14. The V_2 voltage of each layer before and after assembling the 40-turn C2 magnet. 77 K, self-field. Data points: measurement. Lines: fitting of the measurements according to (1). Open circles and dashed lines: measurement of each layer stand-alone. Closed circles and solid lines: measurement after the assembly into the C2 magnet. Layer number is shown next to the lines.

Table 5. I_c and n-value of each layer of the 40-turn C2 magnet before assembly, after assembly at 77 and 4.2 K. The voltage criterion is 20 μV.

Layer	77 K #1 stand-alone		77 K #2 assembled		4.2 K assembled		4.2 K/77 K ratio
	I_c (A)	n (-)	I_c (A)	n (-)	I_c (A)	n (-)	(-)
1	647	7.8	464	7.8	4,670	6.7	10.1
2	740	9.3	640	4.7	5,688	8.0	8.9
3	829	13.2	600	11.2	6,533	18.3	10.9
4	434	3.1	367	7.6	4,338	9.6	12.0

Figure 17 shows the load lines for the C2 magnet and the $I_c(B)$ of the Layer 1 witness sample measured at 4.2 K with a voltage criterion of 20 μV. At this voltage level, the C2 magnet is expected to generate a dipole field of 3.02 T at 6.392 kA.

4.2.3. Degradation of critical current in Layer 1 after thermal runaway To probe the true magnet performance, we increased the peak current by increasing the voltage threshold for the quench detection for each subsequent current ramp. For the first 11 ramps, the voltage across Layer 4 triggered the quench detection system with a threshold voltage level from 90 μV to 1.32 mV. The voltage across Layer 1 started running away and triggering the quench detection in Ramp 12 with a threshold voltage of 400 μV. To further increase the peak current, we increased the threshold voltage for Layer 1 to 600 μV in Ramp 13. The $V(I)$ curves of each layer reproduced themselves for the first 13 ramps (figure 18).

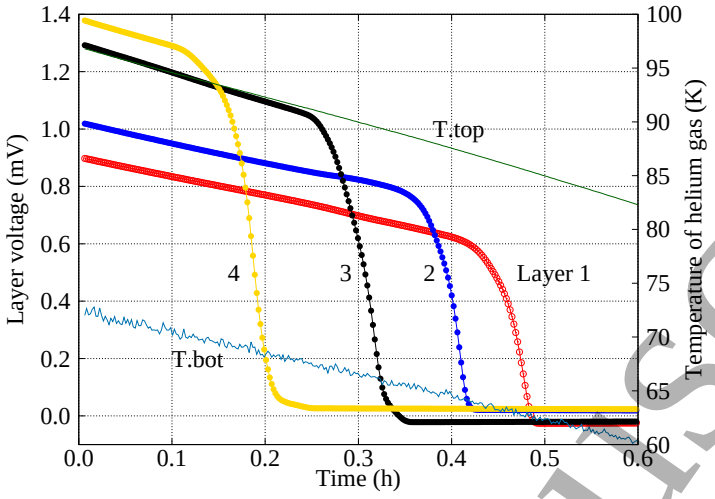

Figure 15. The superconducting transition of each layer in the C2 magnet during the cooldown to 4.2 K. The readings from the top and bottom temperature sensors are shown in the secondary y-axis.

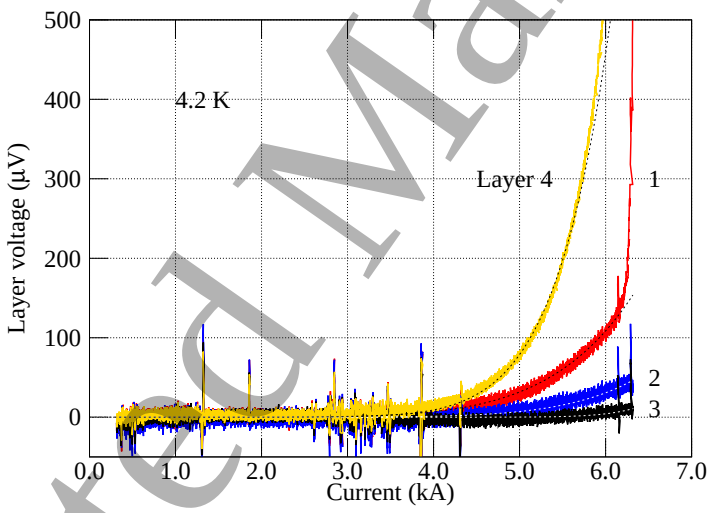

Figure 16. The $V(I)$ of each layer during a ramp at 4.2 K. The dashed lines are the exponential fits of the voltage data according to (1). The spikes were inductive voltages due to ramp-rate irregularities.

Ramp 14 showed that the I_c of Layer 1 decreased by 5% from 4.670 to 4.453 kA, defined at 20 μV, and the n-value increased by 18% from 6.7 to 7.9 (figure 18). No further degradation was observed in Ramp 15. The other three layers did not show any obvious degradation.

Layer 1 voltage reached at least 0.6 V during Ramp 13, saturating the input of the data acquisition system. Figure 19 shows the voltages across Layer 1 during Ramps 12 and 13, with the resistive components during the current decay shown as dashed lines. Integrating the magnet current and resistive voltage, the Joule heating generated in Layer 1 was about 815 J for Ramp 13 during the period when the current decayed from its peak value to zero (from 0 to 1 s in figure 19). The Joule heating was about 27 J for

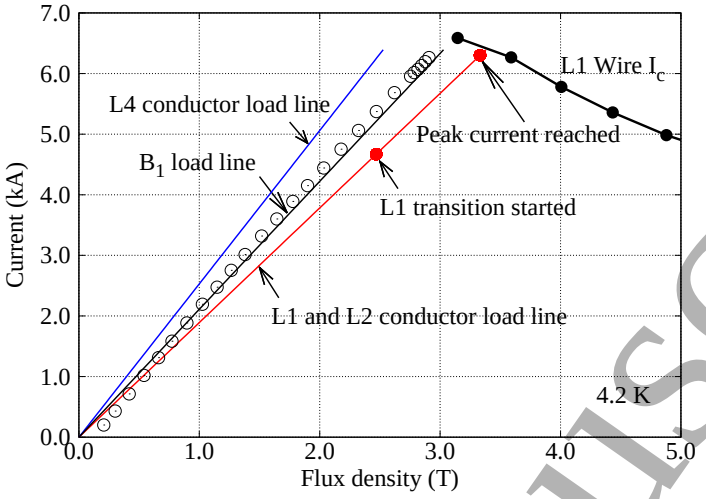

Figure 17. The load lines for the C2 magnet at 4.2 K and the dipole field measured with the rotating coil (open circles). The I_c of the Layer 1 witness sample was defined at a voltage criterion of 20 μV (19.8 μV m^{-1}). Layer 1 started transitioning at 4.670 kA, 73% of SSP, and reached 6.290 kA and a maximum dipole field of 2.91 T (figure 16). The conductor load line for Layer 3, not shown here, is close to the load line for the aperture dipole field (B_1).

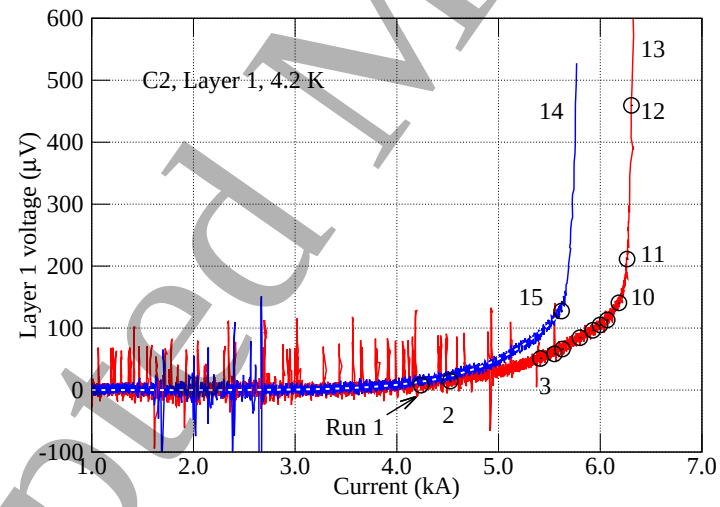

Figure 18. The $V(I)$ of Layer 1 from various ramps at 4.2 K. The open circles represent the peak current/voltage of each ramp except for Ramps 13 and 14. Layer 1 degraded during the thermal runaway of Ramp 13 (red solid line), as evidenced by the early transition in Ramp 14 (blue solid line). The white dashed line is the exponential fit of Ramp 14 according to (1).

Ramp 12 during the current decay.

The I_c degradation in Layer 1 was also confirmed during the 77 K test following the 4.2 K test where the I_c of Layer 1 decreased by 8%, defined at 20 μV, and the n-value increased by 22% compared to the first 77 K test (figure 20). No significant change was measured in the I_c of Layer 4 compared to the previous 77 K test.

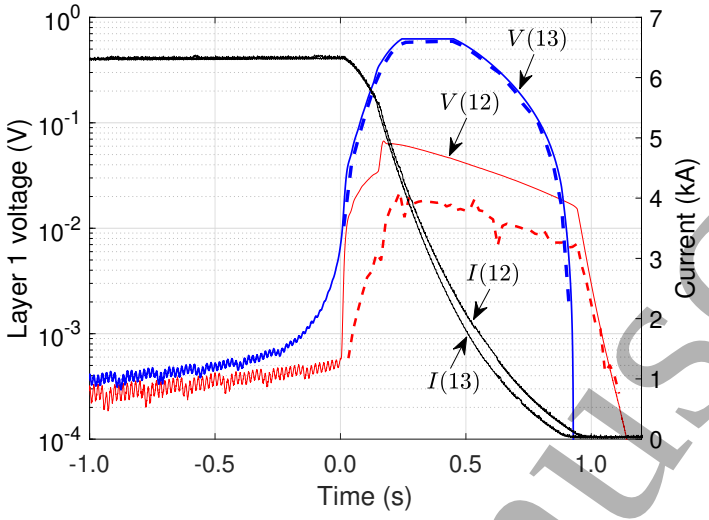

Figure 19. Voltage across Layer 1, in log scale, and magnet current during Ramps 12 and 13. Current decay started at time 0. The dashed lines are the resistive voltage component during the current decay, after removing the inductive component from the measured layer voltage.

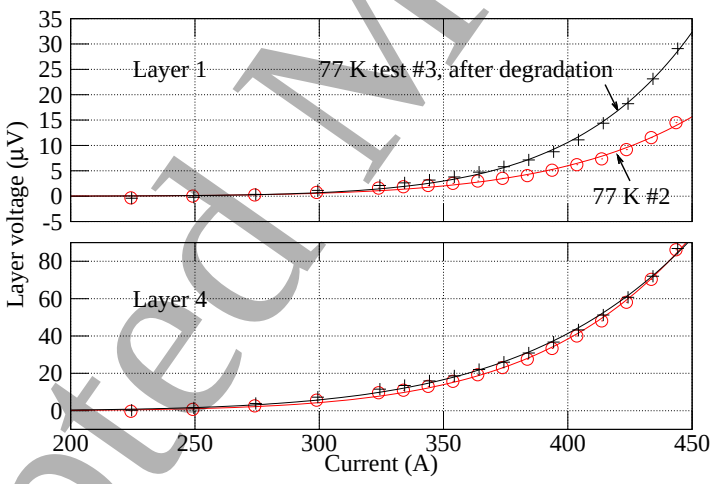

Figure 20. The $V(I)$ of Layers 1 and 4 measured at 77 K, self-field. Cross: measurements after the 4.2 K degradation. Circle: measurements before the degradation. Lines are the exponential fit of the experimental data according to (1).

4.3. Electrical resistance across the joints between layers

Figure 21 shows the voltage across the inter-layer joints of the C2 magnet as a function of current at 77 and 4.2 K. The resistances varied from 7 to 22 nΩ at 4.2 K. Table 6 lists the joint resistances of the three-turn subscale and C2 magnets. The joint resistances reduced by a factor of 8 to 10 from 77 to 4.2 K except for that between Layers 2 and 3 of the three-turn subscale magnet. The joint resistances did not change after the degradation of Layer 1 at 4.2 K.

An industrial computed tomography (CT) scan was performed on a practice

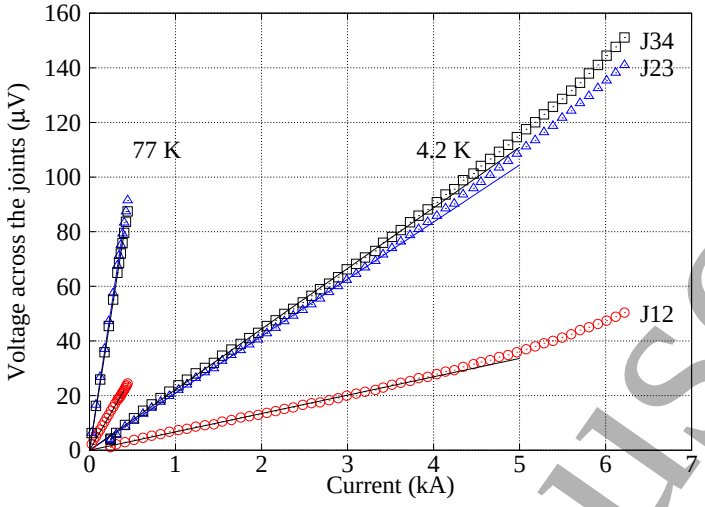

Figure 21. Voltage across the inter-layer joints of the C2 magnet as a function of current at 77 and 4.2 K. The solid lines are the linear fit of the measured data. Their slope gives the joint resistance.

Table 6. The resistance of inter-layer joints in nΩ for the three-turn subscale and C2 magnets at 77 and 4.2 K.

	Three-turn subscale			40-turn C2		
	77 K (nΩ)	4.2 K (nΩ)	ratio (-)	77 K (nΩ)	4.2 K (nΩ)	ratio (-)
Joint 2/1	181	21	8.6	55	7	7.9
Joint 3/2	14	5	2.8	206	21	9.8
Joint 4/3	69	8	8.6	198	22	9.0

termination to help understand its quality. Figure 22 shows an example cross sectional image of the termination towards the CORC® wire. Voids appeared between tapes and between the tape and inner surface of the Cu tube. Voids were found along the termination with volumes ranging from less than 1 mm^3 to a few cubic mm.

4.4. Field quality

The magnetic field in the aperture is expressed as a multipole expansion, given by

$$B_y + iB_x = B_1 \times 10^{-4} \sum_{n=1}^{\infty} (b_n + ia_n) \left(\frac{x+iy}{R_{\text{ref}}} \right)^{n-1}, \quad (2)$$

where b_n is the normal and a_n is the skew multipole coefficient of order n [38, 39]. Both coefficients, normalized to the dipole field (B_1), are expressed in units (10^{-4}) at a reference radius (R_{ref}) of 21.55 mm, covering 55% of the aperture determined by the Layer 1 wire (table 2).

Figure 23 compares the dipole transfer function along the magnet measured at 280, 77 and 4.2 K. Figure 24 compares the normal sextupole (b_3). Also shown are the

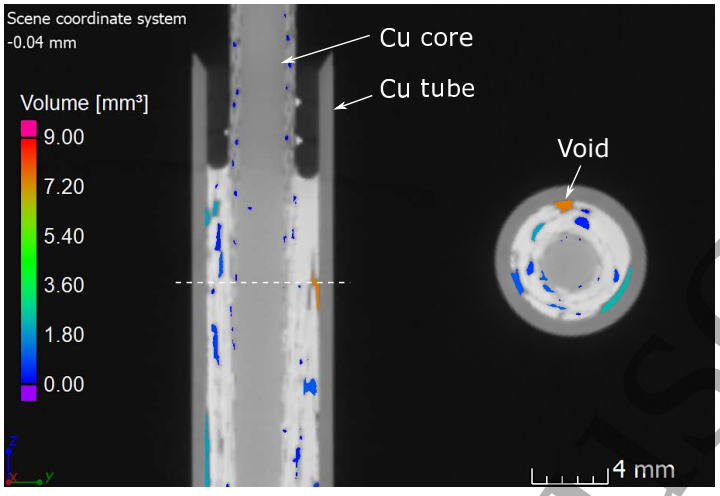

Figure 22. CT images of a practice CORC® termination. Only the portion close to the CORC®-wire end is shown. Left: a longitudinal cross section. Right: the transverse cross section at the longitudinal location as indicated by the dashed line. The gray regions are the Cu tube and core. The white regions are REBCO tapes and indium solder. All other colored regions are voids. The scale of the void volume is shown in the figure.

calculated dipole transfer function and b_3. The calculation is based on the as-designed conductor positioning and does not consider the contribution from the persistent-current effects from the REBCO conductor.

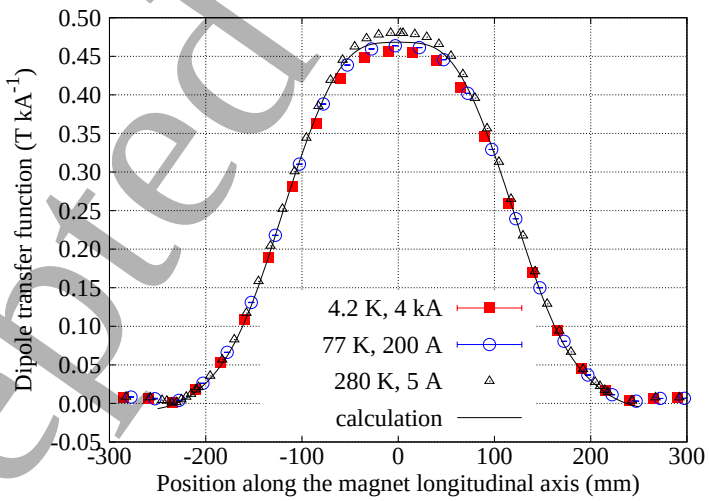

Figure 23. The measured and calculated dipole transfer function along the magnet at 280 K with a current of 5 A, 77 K with 200 A and 4.2 K with 4 kA.

Figure 25 shows the dipole transfer function and normal sextupole (b_3) at 4.2 K at different ramp rates ranging from 50 to 300 A s^{-1}. No obvious ramp-rate dependence was observed in other allowed terms such as b_5 and b_7. The non-allowed terms showed a ramp-rate dependence, however, in particular the skew terms of the odd order such

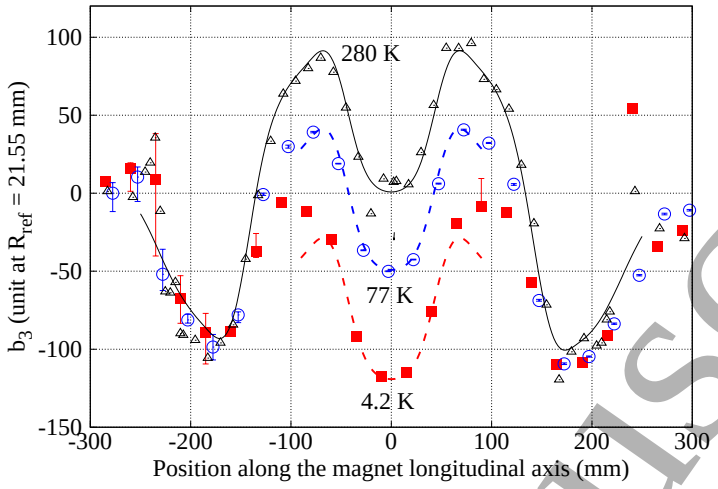

Figure 24. The measured and calculated normal sextupole (b_3) along the magnet at 280 K with a current of 5 A (black triangle), 77 K with 200 A (blue circle) and 4.2 K with 4 kA (red square). The calculation (solid line) was shifted by −50 units to match the 77 K measurement and by −119 units to match the 4.2 K measurement.

as a_3 and a_5. Figure 26 shows an example of a_3. A similar ramp-rate dependence was also observed at 77 K.

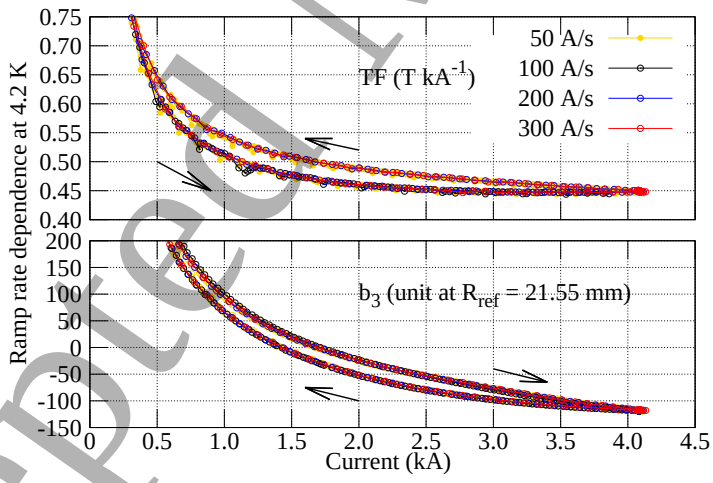

Figure 25. The negligible ramp-rate dependence of the dipole transfer function and normal sextupole (b_3) measured between 0.3 and 4.1 kA at 4.2 K. The arrows indicate the change of TF and b_3 as the current increased and decreased.

5. Discussion

5.1. CORC®-based CCT magnet technology

The four-layer C2 magnet generated a maximum dipole field of 2.91 T at 6.290 kA, 4.2 K, 98% of the 3 T target. We were able to measure the true magnet performance that was

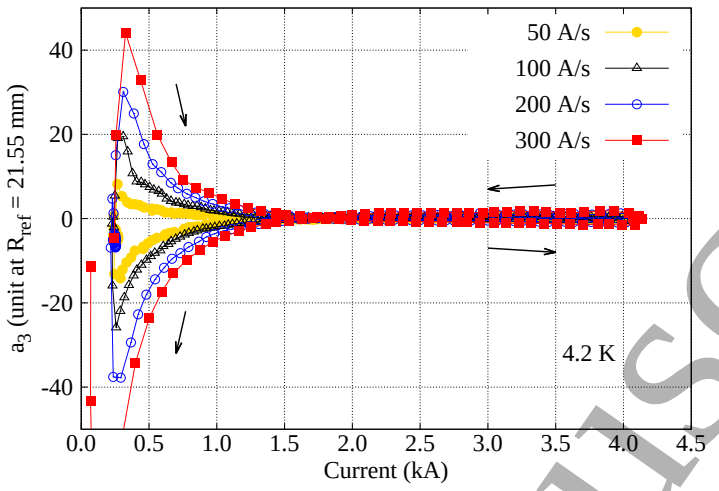

Figure 26. The measured skew sextupole (a_3) during the ramping of the magnet current between 0.3 and 4.1 kA at different rates at 4.2 K. The arrows indicate the change of a_3 as the current increased and decreased.

limited by Layer 1, the inner-most layer, as expected from the peak field and minimum bending radius of the wire (table 2). Despite the low current-carrying capability of Layer 4, the expected magnet performance indicated that the implementation of the new technology features in the C2 magnet was successful.

The half-depth radial grooves allowed for winding CORC® wires under tension with the existing winding table. It also permitted convenient mandrel machining with a four-axis CNC machine. Winding with the full-depth radial groove, however, remains an area of future investigation.

We constrained the CORC® wires by applying wet Stycast, fiberglass tape and release-coated heat-shrink tape. The observed I_c reduction associated with the application of Stycast was likely caused by a change in strain state of the REBCO tapes after cooldown. Although this manual procedure successfully constrained the CORC® wires without introducing significant I_c reduction, it has a few drawbacks that need to be addressed. For instance, air can be trapped when applying Stycast, leaving voids between the conductor and mandrel where the conductor will not be effectively supported by the mandrel. In addition, the manual procedure does not guarantee a consistent and reproducible application of Stycast for all four layers. For a more reproducible and scalable application of epoxy for future magnets, a vacuum impregnation technique compatible with CORC® wires must be selected.

The C2 magnet was wound with a total of 70 m of commercial CORC® conductor, up from 30 m for the C1 magnet [31]. The wires for the inner three layers of the C2 magnet clearly showed a consistent transport performance (figure 14). This suggests that a reasonably uniform performance can be achieved over at least 47 m section of 30-tape CORC® wires, increasing the confidence level for the performance of future long CORC® wire production required for magnet applications (on the order of 100 m).

The C2 magnet showed no training behavior as evidenced by the reproducible $V(I)$

traces (figure 18). Absence of training was observed in other CORC® magnets including a solenoid magnet tested in a background field of 14 T [31, 40]. The transition behavior of the C2 magnet showed that one can repeatedly drive the magnet into the flux-flow regime with an engineering current density between 400 and 550 A mm^{-2} at 4.2 K. The slow resistive-voltage rise also provided precious time to detect the transition and protect the magnet.

The different amplitudes of the inductive voltage noise in the three-turn subscale magnet highlighted the need to completely co-wind the instrumentation wires along the CORC® wire [22, 40–42]. The co-wound instrumentation wires across each layer yielded low-noise voltage signals for reliable quench detection, allowing us to raise the layer voltage in a controlled way until the thermal runaway.

Testing at 77 K provided early feedback on a coil performance. All the coils in the subscale and C2 magnets showed a consistent ratio between the I_c at 77 and 4.2 K (tables 4 and 5). This suggests that testing at 77 K which requires less time and expense than testing at 4.2 K can become an effective quality control tool for the development of REBCO magnets. Thus, establishing a more accurate prediction on the coil performance at 77 K would be useful, although it would require knowledge of the in-field performance of the REBCO tapes at 77 K and how this would vary between tape batches.

The inter-layer joints demonstrated acceptable resistances that allowed us to test the magnet performance without excessive heat generation in the joints; in some cases they were lower than 10 nΩ at 4.2 K. The reduction of the joint resistance from 77 to 4.2 K was consistent with a residual resistivity ratio (RRR) of 50 – 100 for the Cu components in the inter-layer joints. The variation among the joint resistances needs to be understood. In the future, we expect to further reduce the joint resistance by minimizing the void volume inside the termination as shown in figure 22. The contact resistance between the Cu termination and Cu blocks could be reduced by using indium wire or indium foil that has minimum surface oxide layer. Another option is to solder the Cu termination to Cu blocks without using indium wire or foil in between. The impact of tape substrate and interfacial resistances inside REBCO tapes also needs to be understood [43–45].

5.2. Feedback on CORC® wire development

The main reason that prevented the C2 magnet from reaching a higher field was that the in-field performance of the REBCO tapes could not be specified and turned out to be below average. This required us to optimize each CORC® wire to reach I_c at the same current, although each wire would experience a different local magnetic field. Future MDP magnets will require higher tape performance. SuperPower Inc. has now allowed us to specify the tape performance at 4.2 K at 6 T for a competitive price, which should significantly reduce the risk of the magnet program.

The relatively low I_c in Layer 4 was likely caused by the combination of tapes with high variation in tape properties such as I_c, causing the initial voltage rise at

relatively low current. A mix of tapes with different properties such as I_c or contact resistance can reduce both the n-value and the current-carrying capability of the multi-tape wire [46, 47]. Indeed, the n-value of Layer 4 before assembly was less than 40% of those of the other three layers (table 5). More research is required to clarify the impact of the mix of tapes with different properties on the resulting cable performance.

The average I_c reduction of 27% at 77 K after winding (table 4) was due to contributions from two effects. First, excessive strains degraded REBCO tapes when the CORC® wire was bent to a small radius [32]. ACT compared the I_c of individual tapes extracted from the CORC® wire in the pole and midplane regions from a previous 3-turn coil (C0b). Similar to the C2 conductor, the wire had 29 tapes and was bent to a minimum radius of 30 mm at the pole region [48]. The sum of the I_c of individual tapes at 76 K from the pole region was about 80% of that from the midplane with minimum bending. This indicated that the bending can cause around 20% I_c reduction that is irreversible due to tape degradation. To minimize the I_c reduction due to irreversible tape degradation, more flexible CORC® wires should be developed (more discussion below).

Second, the CORC® wire experienced a higher magnetic field after winding compared to the self-field of the wire before winding. ACT measured a segment of C2 wire at 76 K as a function of magnetic fields transverse to the longitudinal axis of the wire. The wire I_c reduced by 16% from self-field to an applied field of 100 mT, roughly the peak field transverse to the wire axis ‡ for each three-turn coil stand-alone at their I_c.

The additional I_c reduction after assembly (tables 4 and 5) was also due to the increased magnetic field on the CORC® wire. Table 7 lists the peak magnetic field transverse to the longitudinal axis of the CORC® wire at the I_c of each layer for both the three-turn subscale and 40-turn C2 magnets.

Given the C2 magnet aperture, the 30 mm minimum bending radius of the CORC® wires led to a tilt angle of 50° for Layers 1 and 2. This is inefficient as these two layers generated more solenoid field than dipole field. Layers 3 and 4 are more efficient thanks to the larger mandrel radii (table 2). For CCT dipole magnets with an aperture of 180 mm or larger, the 30 mm minimum bending radius is excellent as it allows a tilt angle of 20°, below which the dipole transfer function plateaus. For magnets with a smaller aperture, the minimum bending radius should be further improved. A target minimum bending radius is 15 mm for a CCT dipole insert magnet with an inner diameter of 50 mm and an outer diameter of 120 mm [48].

One of the goals for REBCO CCT magnet technology is to reach a 20 T dipole field by generating at least 5 T in a background field of 15 T or higher. Using commercial REBCO tapes with a 25 μm thick substrate, ACT demonstrated a transport performance in a CORC® wire extrapolating to 4,150 A (450 A mm^{-2}) at 4.2 K, 20 T

‡ At 77 K, the Zr-doped REBCO tapes have a minimum I_c when the angle between the applied field and tape broad surface is between 0 and 90 degrees. Therefore, the use of the field transverse to the wire axis is only an approximation to the field that limits the wire performance at 77 K.

Table 7. Peak magnetic field transverse to the longitudinal axis of the CORC® wire in each layer at the measured I_c at 77 K. The I_c reduction after assembly with respect to the stand-alone case was determined from tables 4 and 5.

Magnet	Layer	Stand alone (mT)	After assembly (mT)	I_c reduction after assembly
3-turn	1	116	183	22%
	2	108	183	24%
	3	100	135	29%
	4	∼102	132	17%
40-turn	1	124	245	28%
	2	145	339	14%
	3	156	279	28%
	4	83	145	15%

and with a 31.5 mm bending radius [15]. However, there is still a significant gap between state-of-the-art and the required CORC® wire performance for a REBCO CCT insert magnet [48]. A possible path towards achieving the target performance in CORC® wires is to develop thinner and narrower REBCO tapes [49] and to improve their transport performance at relevant field and 4.2 K [10].

The field-quality study of the C2 magnet showed two features relevant for the conductor development. The first feature is the large values of the allowed high-order harmonics (b_3 and b_5) that can be attributed to the persistent-current effects in REBCO layers. The effect was also seen in a CORC® solenoid magnet tested in a 14 T background field [40]. Since the priority is to push the maximum dipole field by further increasing the wire transport performance, we can reduce the magnetization effects with a narrower REBCO layer [50, 51] and passive correction [52].

The second feature is the ramp-rate dependence of specific field errors (figure 26). The possible eddy currents induced in the metal mandrel cannot solely explain this because the C1 magnet with a non-metal mandrel showed a similar behavior. The distribution of the current density in REBCO layer driven by different ramp rates of the current can lead to a similar ramp-rate dependence [53]. The behavior also resembled those of LTS accelerator magnets fabricated from Rutherford cables where inter-strand coupling currents contributed to the ramp-rate dependence [54–56].

If the inter-tape coupling currents lead to the ramp-rate dependence in the C1 and C2 magnets, it would suggest that the contact resistances between the as-received REBCO tapes in a CORC® wire can be low enough to allow current flowing between tapes, consistent with the turn-to-turn coupling currents in non-insulated REBCO coils [57–59]. Then, further reduction of contact resistance by using, for example, pre-tinned tapes, can lead to more pronounced and undesired ramp-rate dependence [60]; and control of inter-tape contact resistance may be necessary [61–63]. More detailed

studies are required to clarify the source of the observed ramp-rate dependence and its implications on conductor optimization.

5.3. Conductor degradation during thermal runaway and the need to understand the cause of superconducting-to-normal transition

Layer 1 conductor degraded when we tested the limit of the magnet performance. The degradation was likely caused by heating during the thermal runaway when the Cu stabilizer in CORC® wire carried the current. Under an adiabatic condition, the Joule heating of 815 J during the thermal runaway can raise the temperature of a 10 cm long CORC® wire from 4.2 to 500 K (figure 27), a temperature at which similar I_c degradation is observed in single tapes [64, 65]. The quench-integral method [66] gave a similar peak temperature of 500 K assuming a RRR of 35 for the Cu in the wire [67]. In ramps prior to Ramp 13, the estimated peak temperature was below 127 K (figure 27).

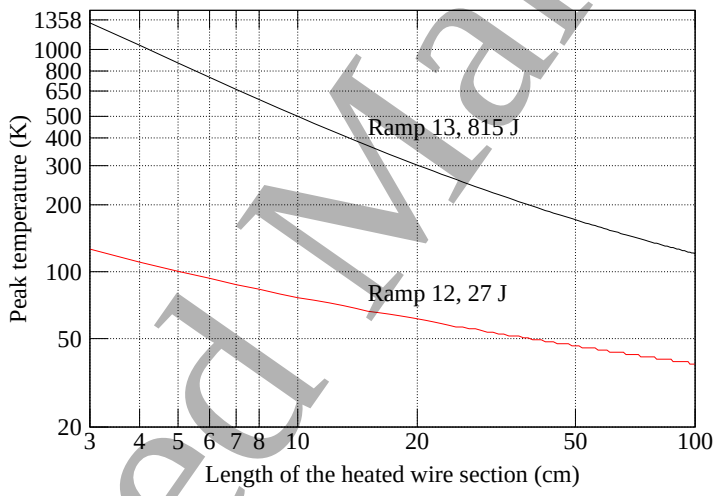

Figure 27. The temperature that a certain length of CORC® wire in Layer 1 can reach given 815 J of heating in Ramp 13 and 27 J of heating in Ramp 12, assuming the energy is absorbed by the CORC® wire with an initial temperature of 4.2 K. Log-log scale.

The assumption of about 10 cm long or less of the heated section is reasonable considering a previous coil (C0b) wound with a 29-tape CORC® wire that was damaged during an unprotected quench [48]: a 5 mm long wire segment evaporated and the scorch mark due to heating covered a 20 cm long wire section.

The adiabatic assumption can be justified by the Stycast impregnation and limited cooling for Layer 1. The radial clearance in the raised ends between Layer 1 and Layer 2 was about only 50 μm filled with Kapton tapes, except for seven grooves in the raised ends (figure 6). The aperture of Layer 1 was occupied by the anticryostat with a radial clearance of 0.75 mm between the ID of Layer 1 and OD of the anticryostat. Both factors can lead to limited cooling for Layer 1, which was evidenced by the sequential superconducting transitions from Layers 4 to 1 during the cooldown (figure 15). More

effective cooling of Layer 4 may have contributed to its absence of thermal runaway despite its early transition.

A fast energy extraction from the magnet is necessary to minimize the localized heat dissipation and degradation in CORC® wires. The similar decay rate of the current between Ramps 12 and 13 (figure 19) indicated that the resistive normal zone itself in the C2 magnet, even catastrophic enough to degrade the wire, was insufficient to drive a fast current decay due to the stationary normal zone in REBCO conductors. An external dump resistor should be implemented in addition to potential schemes to heat the entire coil.

Thermal runaway should be avoided by early detection of the superconducting-to-normal transition in REBCO magnets. This is possible, as the C2 magnet clearly showed, thanks to clear voltage rise well above the noise floor before thermal runaway occurred (figure 18). The test of the recent REBCO solenoid wound with a 28-tape CORC® conductor also demonstrated a gradual transition behavior in a background field of 14 T and the reliable transition detection with co-wound voltage tap wires [40]. The recent Feather dipole magnet based on REBCO Roebel cables provides another example [22]. The quench protection of larger-scale REBCO magnets based on multi-tape conductors can be less challenging if they show a similar gradual transition that can be reliably detected well before thermal runaway. Alternative transition detection methods should be developed and evaluated [68–72] while we investigate the feasibility of voltage-based detection for magnets with longer conductors operating in strong electromagnetic background noise [42].

Although the voltage signal worked well for detecting superconducting-to-normal transitions in the C2 magnet, it does not tell us from where along the conductor the transition occurred. This knowledge is critical to understand and address the causes of transition and to further improve the magnet and conductor technology. One question is why Layer 1 started the transition at 73% of the short-sample prediction (figure 17). There are three possible explanations. First, the wire performance varied along the wire and cannot be represented by a short witness sample. Second, the witness sample represented the uniform performance of a long wire but the wire degraded during magnet fabrication. Third, the wire had a uniform performance as represented by the witness sample, and multiple segments in the wire transitioned simultaneously §. For instance, transitions may occur in multiple pole regions where the wire is bent to the smallest bending diameter that results in local I_c degradation of the CORC® wire. In all these cases, we need to identify locations of first onset of flux-flow voltage to understand the cause of transition [68, 69].

§ Suppose the short witness sample transitions at I_c. If the long wire has m segments transitioning simultaneously as the witness sample does, then the long wire will start transitioning at $I_c/\sqrt[n]{m}$ with the same n-value as the witness sample. Here, the witness sample (at 2.5 T background field) and Layer 1 wire both had an n-value of 6.7. A simultaneous transition of eight short-sample segments ($m = 8.2$) in Layer 1 can explain the transition at 73% of witness sample I_c.

6. Conclusion

The four-layer C2 dipole magnet represented another successful step towards the development of high-field CORC®-based CCT accelerator magnet technology. The magnet reached a maximum dipole field of 2.91 T at 4.2 K. A total of 100 m of 30-tape CORC® wire was manufactured for the C2 magnet project, consuming 5 km of REBCO tape with a 30 μm thick substrate manufactured by SuperPower Inc. Wire sections were wound onto printed Accura® Bluestone™ and machined aluminum bronze mandrels with half-depth radial grooves under a tension of 30 N. Stycast epoxy was applied after winding to constrain the wires. A three-turn subscale magnet showed an average of 27% I_c reduction at 77 K after winding with a minimum bending radius of 30 mm. The C2 magnet showed that one can repeatedly drive the magnet into the flux-flow regime, resulting in a reproducible transition behavior without training at an engineering current density between 400 and 550 A mm^{-2} at 4.2 K, allowing reliable quench detection. Meanwhile, a thermal runaway should be avoided and the magnet should be adequately protected to prevent conductor degradation.

The test results of the C2 magnet emphasized two critical development needs. One is that the current-carrying capability and flexibility of the CORC® wires be further improved to enable high-field dipole insert magnet applications. Highly localized conductor damage, such as likely occurred at the poles of the CCT magnet, should be avoided to allow operation closer to the maximum CORC® wire capability while reducing local heat dissipation that may ultimately result in a thermal runaway that can degrade the magnet. The other need is to identify locations of first onset of flux-flow voltage to understand and address the factors that limit the conductor and magnet performance.

Acknowledgments

We thank David Larbalestier, Van Griffin, James Maddox and James Gilman of National High Magnetic Field Laboratory for providing a cryostat to test the magnet. We thank Aurelio Hafalia, Reginald Lee, Thomas Lipton, and Li Wang of LBNL for preparing the cryostat for the test; we thank Thomas Lipton for arranging the five-axis CNC machining of a metal mandrel with tilted grooves; and we also thank Drew Hazelton of SuperPower Inc. and Kenneth Marken of U.S. Department of Energy for useful discussions.

This work was supported by the U.S. Magnet Development Program through Director, Office of Science, Office of High Energy Physics and by the Office of Fusion Energy Sciences of the US Department of Energy under Contract No. DEAC02-05CH11231. The work was also supported by the US Department of Energy under contracts DE-SC0014009 and DE-SC0015775. CSM was supported by the DOE Office of Science Graduate Student Research Program, Advanced Technology Research and Development in High Energy Physics.

References

[1] Scanlan R M, Dietderich D R, Higley H C, Marken K R, Motowidlo L R, Sokolowski R and Hasegawa T 1999 *IEEE Trans. Appl. Supercond.* **9** 130–133

[2] Godeke A, Cheng D, Dietderich D R, Ferracin P, Prestemon S O, Sabbi G and Scanlan R M 2007 *IEEE Trans. Appl. Supercond.* **17** 1149–1152

[3] Larbalestier D C, Jiang J, Trociewitz U P, Kametani F, Scheuerlein C, Dalban-Canassy M, Matras M, Chen P, Craig N C, Lee P J and Hellstrom E E 2014 *Nat. Mater.* **13** 375–381

[4] Zhang K, Higley H, Ye L, Gourlay S, Prestemon S, Shen T, Bosque E, English C, Jiang J, Kim Y, Lu J, Trociewitz U, Hellstrom E and Larbalestier D 2018 *Superconductor Science and Technology* **31** 105009

[5] Garcia Fajardo L, Brouwer L, Caspi S, Hafalia A, Hernikl C, Prestemon S, Shen T, Bosque E and English C 2019 *IEEE Trans. Appl. Supercond.* **29** 4002005

[6] Shen T, Bosque E, Davis D, Jiang J, White M, Zhang K, Higley H, Turqueti M, Huang Y, Miao H, Trociewitz U, Hellstrom E, Parrell J, Hunt A, Gourlay S, Prestemon S and Larbalestier D 2019 *Scientific reports* **9** 10170

[7] Wang X, Gourlay S A and Prestemon S O 2019 *Instruments* **3** 62

[8] Shen T and Garcia Fajardo L 2020 *Instruments* **4** 17

[9] Marken K 2012 Fundamental issues in high temperature superconductor (HTS) materials science and engineering *High Temperature Superconductors (HTS) for Energy Applications* Woodhead Publishing Series in Energy ed Melhem Z (Woodhead Publishing) pp 3 – 33 ISBN 978-0-85709-012-6

[10] Majkic G, Pratap R, Xu A, Galstyan E, Higley H, Prestemon S, Wang X, Abraimov D, Jaroszynski J and Selvamanickam V 2018 *Superconductor Science and Technology*

[11] Goldacker W, Grilli F, Pardo E, Kario A, Schlachter S I and Vojenčiak M 2014 *Superconductor Science and Technology* **27** 093001

[12] Takayasu M, Chiesa L, Bromberg L and Minervini J V 2012 *Superconductor Science and Technology* **25** 014011

[13] Solovyov V and Farrell P 2016 *Superconductor Science and Technology* **30** 014006

[14] van der Laan D C, Weiss J D and McRae D M 2019 *Superconductor Science and Technology* **32** 033001

[15] Weiss J D, van der Laan D C, Hazelton D, Knoll A, Carota G, Abraimov D, Francis A, Small M A, Bradford G and Jaroszynski J 2020 *Superconductor Science and Technology* **33** 044001 ISSN 0953-2048

[16] Kar S, Sandra J S, Luo W, Kochat M, Jaroszynski J, Abraimov D, Majkic G and Selvamanickam V 2019 *Superconductor Science and Technology* **32** 10LT01 ISSN 0953-2048

[17] Badel A, Ballarino A, Barth C, Bottura L, Dhalle M M J, Fleiter J, Goldacker W, Himbele J, Kario A, Rossi L, Rutt A, Scheuerlein C, Senatore C, Tixador P, Usoskin A and Yang Y 2016 *IEEE Trans. Appl. Supercond.* **26** 4803908

[18] Uglietti D 2019 *Superconductor Science and Technology* **32** 053001 ISSN 0953-2048

[19] Durante M, Borgnolutti F, Bouziat D, Fazilleau P, Gheller J M, Molinié F and Antoni P D 2018 *IEEE Trans. Appl. Supercond.* **28** 4203805

[20] Borgnolutti F, Durante M, Debray F, Rifflet J M, Rijk G D, Tixador P and Tudela J M 2016 *IEEE Trans. Appl. Supercond.* **26** 4602605

[21] Kirby G, van Nugteren J, Ballarino A, Bottura L, Chouika N, Clement S, Datskov V, Fajardo L, Fleiter J, Gauthier R, Gentini L, Lambert L, Lopes M, Perez J, de Rijk G, Rijllart A, Rossi L, ten Kate H, Durante M, Fazilleau P, Lorin C, Haro E, Stenvall A, Caspi S, Marchevsky M, Goldacker W and Kario A 2015 *IEEE Trans. Appl. Supercond.* **25** 4000805

[22] van Nugteren J, Kirby G, Bajas H, Bajko M, Ballarino A, Bottura L, Chiuchiolo A, Contat P A, Dhallé M, Durante M, Fazilleau P, Fontalva A, Gao P, Goldacker W, ten Kate H, Kario A, Lahtinen V, Lorin C, Markelov A, Mazet J, Molodyk A, Murtomäki J, Long N, Perez J, Petrone C, Pincot F, de Rijk G, Rossi L, Russenschuck S, Ruuskanen J, Schmitz K, Stenvall A, Usoskin A, Willering G and Yang Y 2018 *Superconductor Science and Technology* **31** 065002

[23] Rossi L, Badel A, Bajas H, Bajko M, Ballarino A, Barth C, Betz U, Bottura L, Broggi F, Chiuchiolo A, Dhallé M, Durante M, Fazilleau P, Fleiter J, Gao P, Goldacker W, Kario A, Kirby G, Haro E, Himbele J, Lorin C, Murtomaki J, van Nugteren J, Petrone C, de Rijk G, Ruuskanen J, Senatore C, Statera M, Stenvall A, Tixador P, Yang Y, Usoskin A and Zangenberg N 2018 *IEEE Trans. Appl. Supercond.* **28** 4001810

[24] Gourlay S A, Prestemon S O, Zlobin A V, Cooley L and Larbalestier D 2016 The U.S. magnet development program plan `https://escholarship.org/uc/item/5178744r`

[25] Meyer D and Flasck R 1970 *Nuclear Instruments and Methods* **80** 339–341

[26] Gavrilin A V, Bird M D, Bole S T and Eyssa Y M 2002 *IEEE Trans. Appl. Supercond.* **12** 465–469

[27] Goodzeit C L, Ball M J and Meinke R B 2003 *IEEE Trans. Appl. Supercond.* **13** 1365–1368

[28] Akhmeteli A M, Gavrilin A V and Marshall W S 2005 *IEEE Trans. Appl. Supercond.* **15** 1439–1443

[29] Caspi S, Borgnolutti F, Brouwer L, Cheng D, Dietderich D R, Felice H, Godeke A, Hafalia R, Martchevskii M, Prestemon S, Rochepault E, Swenson C and Wang X 2014 *IEEE Trans. Appl. Supercond.* **24** 4001804 and references therein.

[30] Brouwer L N 2015 *Canted-Cosine-Theta Superconducting Accelerator Magnets for High Energy Physics and Ion Beam Cancer Therapy* Ph.D. thesis University of

California, Berkeley `https://escholarship.org/uc/item/8jp4g75g` (accessed on 17 November 2019)

[31] Wang X, Dietderich D R, DiMarco J, Ghiorso W B, Gourlay S A, Higley H C, Lin A, Prestemon S O, van der Laan D and Weiss J D 2019 *Superconductor Science and Technology* **32** 075002

[32] Weiss J D, Mulder T, ten Kate H J and van der Laan D C 2017 *Superconductor Science and Technology* **30** 014002 and references therein.

[33] van der Laan D 2017 Superconducting cable connections and methods US Patent 9,755,329

[34] Jain A K 1998 Harmonic coils *CERN Accelerator School: measurement and alignment of accelerator and detector magnets* CERN-98-05 pp 175–218

[35] DiMarco J, Chlachidze G, Makulski A, Orris D, Tartaglia M, Tompkins J, Velev G and Wang X 2013 *IEEE Trans. Appl. Supercond.* **23** 9000505

[36] Wang X, Caspi S, Cheng D, Felice H, Ferracin P, Hafalia R, Joseph J, Lietzke A, Lizarazo J, McInturff A, Sabbi G and Sasaki K 2009 Magnetic field measurements of HD2, a high field Nb_3Sn dipole magnet *Proceedings of PAC* p 283

[37] Wang X, Hafalia R, Joseph J, Lizarazo J, Martchevsky M and Sabbi G 2011 A hybrid data acquisition system for magnetic measurement of accelerator magnets Tech. Rep. LBNL-4857E Lawrence Berkeley National Laboratory

[38] Jain A K 1997 Basic theory of magnets *Proceedings of CERN accelerator school on measurement and alighnment of accelerator and detector magnets*

[39] Bottura L 2001 Standard analysis procedures for field quality measurement of the LHC magnets — part I: harmonics Tech. Rep. LHC-MTA-IN-97-007 LHC/MTA

[40] Van Der Laan D C, Weiss J D, Trociewitz U P, Abraimov D, Francis A, Gillman J, Davis D S, Kim Y, Griffin V, Miller G, Weijers H W, Cooley L D, Larbalestier D C and Wang X 2020 *Superconductor Science and Technology* **33** 05LT03 ISSN 0953-2048

[41] Michael P C, Bromberg L, van der Laan D C, Noyes P and Weijers H W 2016 *Superconductor Science and Technology* **29** 045003 ISSN 0953-2048

[42] van der Laan D C, Weiss J D, Scurti F and Schwartz J 2020 *Superconductor Science and Technology* ISSN 0953-2048

[43] Lu J, Han K, Sheppard W R, Viouchkov Y L, Pickard K W and Markiewicz W D 2011 *IEEE Trans. Appl. Supercond.* **21** 3009–3012

[44] Tsui Y, Surrey E and Hampshire D 2016 *Superconductor Science and Technology* **29** 075005

[45] Fleiter J and Ballarino A 2017 *IEEE Trans. Appl. Supercond.* **27** 6603305

[46] Pothavajhala V, Graber L, Kim C H and Pamidi S 2014 *IEEE Trans. Appl. Supercond.* **24** 4800505 ISSN 1051-8223

[47] Araujo Martínez A C, Ji Q, Prestemon S O, Wang X and Maury Cuna G H I 2020 *IEEE Trans. Appl. Supercond.* **30** 6600605 ISSN 1558-2515

[48] Wang X, Caspi S, Dietderich D R, Ghiorso W B, Gourlay S A, Higley H C, Lin A, Prestemon S O, van der Laan D and Weiss J D 2018 *Superconductor Science and Technology* **31** 045007

[49] Anvar V A, Ilin K, Yagotintsev K A, Monachan B, Ashok K B, Kortman B A, Pellen B, Haugan T J, Weiss J D, van der Laan D C, Thomas R J, Jose Prakash M, Hossain M S A and Nijhuis A 2018 *Superconductor Science and Technology* **31** 115006

[50] Kesgin I, Levin G A, Haugan T J and Selvamanickam V 2013 *Appl. Phys. Lett.* **103** 252603

[51] Vojenčiak M, Kario A, Ringsdorf B, Nast R, van der Laan D C, Scheiter J, Jung A, Runtsch B, Gömöry F and Goldacker W 2015 *Superconductor Science and Technology* **28** 104006

[52] Kashikhin V and Zlobin A 2001 *IEEE Trans. Appl. Supercond.* **11** 2058–2061

[53] Amemiya N, Sogabe Y, Sakashita M, Iwata Y, Noda K, Ogitsu T, Ishii Y and Kurusu T 2015 *Superconductor Science and Technology* **29** 024006 ISSN 0953-2048

[54] Verweij A P 1995 *Electrodynamics of Superconducting Cables in Accelerator Magnets* Ph.D. thesis University of Twente `http://inspirehep.net/record/888466` (accessed on 17 November 2019)

[55] Ogitsu T, Kovachev V and Devred A 1997 *Part. Accel.* **57** 215–235 `http://inspirehep.net/record/463305` (accessed on 17 November 2019)

[56] Collings E, Sumption M, Susner M, Dietderich D, Krooshoop E and Nijhuis A 2012 *IEEE Trans. Appl. Supercond.* **22** 6000904

[57] Wang X, Hahn S, Kim Y, Bascuñán J, Voccio J, Lee H and Iwasa Y 2013 *Superconductor Science and Technology* **26** 035012

[58] Suetomi Y, Yanagisawa K, Nakagome H, Hamada M, Maeda H and Yanagisawa Y 2016 *Superconductor Science and Technology* **29** 105002 ISSN 0953-2048

[59] Wang Y, Song H, Yuan W, Jin Z and Hong Z 2017 *Journal of Applied Physics* **121** 113903

[60] Yagotintsev K A, Anvar V A, Gao P, Dhalle M, Haugan T J, van der Laan D C, Weiss J D, Al Hossain M S and Nijhuis A 2020 *Superconductor Science and Technology* ISSN 0953-2048

[61] Lu J, Levitan J, McRae D and Walsh R 2018 *Superconductor Science and Technology* **31** 085006 ISSN 0953-2048

[62] Kovacs C J, Sumption M D, Barzi E Z, Turrioni D, Kashikhin V S, Majoros M and Collings E W 2019 Direct measurement of modified interconductor contact resistance values in coated conductor stacks and roebel cables `https://indico.cern.ch/event/763185/contributions/3416533/` presentation at the International Conference on Magnet Technology

[63] Yang Z, Araujo Martínez A C, Muley S V, Wang X, Ji Q and Anders A 2020 accepted, Journal of Applied Physics

[64] Ishiyama A, Tanaka Y, Ueda H, Shiohara Y, Machi T, Iijima Y, Saitoh T, Kashima N, Mori M, Watanabe T and Nagaya S 2007 *IEEE Trans. Appl. Supercond.* **17** 3509–3512 10.1109/TASC.2007.899708

[65] Wang X, Trociewitz U P and Schwartz J 2011 *Superconductor Science and Technology* **24** 035006

[66] Wilson M N 1983 *Superconducting magnets* (New York: Oxford University Press) chap 9, p 201

[67] Bonura M and Senatore C 2014 *Superconductor Science and Technology* **28** 025001

[68] Scurti F, Ishmael S, Flanagan G and Schwartz J 2016 *Superconductor Science and Technology* **29** 03LT01

[69] Jiang J, Zhao Y, Hong Z, Zhang J, Li Z, Hu D, Qiu D, Zhao A, Ryu K and Jin Z 2018 *IEEE Trans. Appl. Supercond.* **28** 4702105

[70] Marchevsky M and Gourlay S A 2017 *Applied Physics Letters* **110** 012601

[71] Takayasu M 2019 *IEEE Trans. Appl. Supercond.* **29** 4702305

[72] Teyber R, Marchevsky M, Prestemon S, Weiss J D and van der Laan D C 2020 *Superconductor Science and Technology* ISSN 0953-2048